


Hydroacoustic High Absorption with Broadband and Wide-Angle Impedance Matching

Chenkai Liu¹,^{*} Jie Luo,² Xiaozhou Liu^{1,*}, and Yun Lai^{1,†}

¹*MOE Key Laboratory of Modern Acoustics, National Laboratory of Solid State Microstructures, School of Physics, and Collaborative Innovation Center of Advanced Microstructures, Nanjing University, Nanjing 210093, China*

²*School of Physical Science and Technology, Soochow University, Suzhou 215006, China*

 (Received 2 June 2022; revised 12 June 2022; accepted 23 August 2022; published 4 October 2022)

We numerically demonstrate a general method to achieve acoustic high absorption in water with a wide range of incident angles and a broad frequency bandwidth. Different from previous studies considering local resonances with a narrow bandwidth or porous materials with a gradient design, we show that flat multilayer solid composites can be engineered to be perfectly impedance matched with water over a wide range of angles and a broad spectrum. By adding a proper loss factor to the composites, sound waves can be gradually dissipated and high absorption can be realized. Such a method is robust and adaptive to a broad range of material parameters. Our work could promise broad underwater applications.

DOI: [10.1103/PhysRevApplied.18.044008](https://doi.org/10.1103/PhysRevApplied.18.044008)

I. INTRODUCTION

Great demand for hydroacoustic absorption has been increasing with the further development of underwater acoustic stealth [1–4]. There are two key principles for hydroacoustic absorption, one is that the material's characteristic impedance should be matched with that of water to eliminate reflection on the surface, and the other is that the material loss should be large enough to dissipate sound energy inside the material. Porous materials are commonly applied as hydroacoustic absorbers due to their good absorption properties and easy manufacturability. Conventional porous materials include viscoelastic polymers [5–7], porous metals [8–10], and nonmetallic porous materials [11,12]. To overcome the problem of impedance mismatching, porous materials are often engineered with a gradient design [13–15]. Relying on the physical mechanism of intermolecular friction and heat transfer, a bulky size is usually required for porous materials at low frequencies. In addition, based on the multiple scattering effect and mode conversion, local-resonance materials are widely implemented in the field of anechoic coating. The main types of resonance absorber include air-void resonance [16–25] and solid-inclusion resonance [26–33]. Although local-resonance materials greatly improve the low-frequency property, they also suffer from the disadvantage of relatively narrow bandwidth. Other approaches include the utilization of piezoelectric composites [34–37]

and artificial metamaterials [38–40]. A variety of innovative concepts are proposed to improve the hydroacoustic absorption performances; however, the issue of impedance matching between the absorber and water has not been totally explored.

Inspired by ultratransparent artificial metamaterials with broadband and wide-angle impedance-matching properties in both electromagnetics [41–44] and acoustics [45,46], here, we numerically illustrate a general method to realize high acoustic absorption in water by flat multilayer composites. Through an iterative algorithm, the multilayer composite exhibits spatially dispersive effective parameters and its effective impedance can be designed to be perfectly matched with that of water over a wide range of incident angles and a broad frequency bandwidth. As illustrated in Fig. 1, incident sound waves can penetrate into the absorber with very high efficiency on the surface due to the unique impedance-matching property. Then, sound waves are gradually dissipated inside the absorber due to the proper intrinsic material loss. Numerical results provide evidence that the absorptance can approach above 99% for all incident angles of $\pm 70^\circ$. The broadband property is also demonstrated. Moreover, the selection of composite material parameters is flexible in our method.

II. BROADBAND AND WIDE-ANGLE IMPEDANCE MATCHING

First, to exhibit the physical mechanism of the unique impedance-matching property, we begin with a simple multilayer structure, which is symmetric (ABA) with

*xzliu@nju.edu.cn

†laiyun@nju.edu.cn

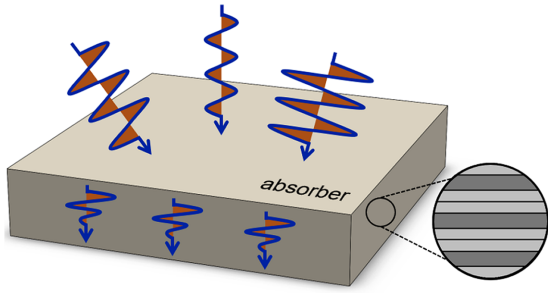


FIG. 1. Illustration of the proposed absorber, which is a kind of composite medium made up of flat multilayer materials. When sound waves impinge on the absorber, reflection is almost eliminated due to the unique impedance-matching property, and the waves are gradually dissipated inside the absorber by the material loss.

a lattice constant of a , as illustrated in the inset in Fig. 2(a). Materials A and B are considered to be known soft porous silicone rubber, the acoustic parameters of which can be easily tuned by its air-filling ratio [47–50].

Because the shear modulus of soft porous silicone rubber is much smaller than its bulk modulus, the influence of the shear modes is negligible in most cases [51]. Here, the parameters of mass density and longitudinal velocity for material A (B) are lossless and chosen as $\rho_A = 1040 \text{ kg/m}^3$ ($\rho_B = 1039 \text{ kg/m}^3$) and $c_A = 1074 \text{ m/s}$ ($c_B = 518 \text{ m/s}$). In addition, the parameters of the background medium, water, are set as $\rho_0 = 1000 \text{ kg/m}^3$ and $c_0 = 1483 \text{ m/s}$. The thickness of each layer is $h_A = 0.309a$ and $h_B = 0.382a$.

Through the pressure acoustics module in COMSOL Multiphysics, the acoustic characteristics of the multilayer composite are obtained. Figure 2(a) shows the equal-frequency contours (EFCs) of the second band of the unit cell. It is seen that the EFCs are almost a part of offset ellipses centered at the X point ($k_x a/\pi = 1$, $k_y a/\pi = 0$). k_x and k_y , respectively, are the wave vectors in the x and y components. Together with the two-dimensional (2D) map of the impedance difference between the composite and water $|(Z_{ABA} - Z_0)/(Z_{ABA} + Z_0)|$ shown in Fig. 2(b), we observe two results. One result is that the

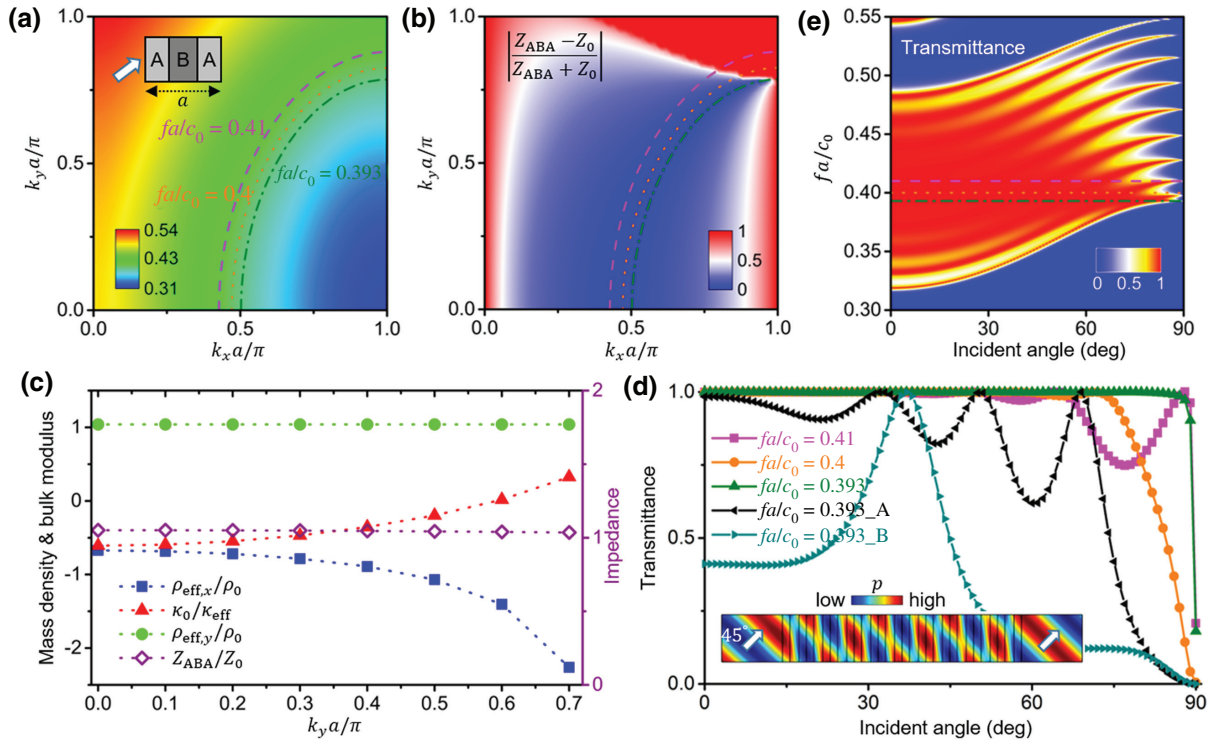


FIG. 2. Physical mechanism of the broadband and wide-angle impedance-matching property. (a) Band structure of a unit cell. Three particular EFCs at three normalized frequencies of $fa/c_0 = 0.393$, 0.4 , and 0.41 are marked. Schematic diagram of a unit cell is illustrated in the inset, and the white arrow denotes the incident wave. (b) Impedance difference between the composite and background medium defined as $|(Z_{ABA} - Z_0)/(Z_{ABA} + Z_0)|$. Blue color indicates matched impedance, while red color represents mismatched impedance. Three lines correspond to three EFCs at $fa/c_0 = 0.393$, 0.4 , and 0.41 . (c) Effective parameters of $\rho_{\text{eff},x}/\rho_0$, $\rho_{\text{eff},y}/\rho_0$, $\kappa_0/\kappa_{\text{eff}}$, and Z_{ABA}/Z_0 as a function of k_y retrieved from the eigenfields at $fa/c_0 = 0.393$. (d) Transmittance as a function of incident angles for the composite with ten unit cells at three frequencies of $fa/c_0 = 0.393$, 0.4 , and 0.41 . Acoustic-pressure-field distribution under plane-wave radiation with 45° incident angle at $fa/c_0 = 0.393$ is shown in the inset. Transmittance curves for contrasts (only A material and only B material) with the same thickness are also plotted. (e) 2D color map for transmittance as a function of incident angles and frequencies. Three lines correspond to three frequencies of $fa/c_0 = 0.393$, 0.4 , and 0.41 .

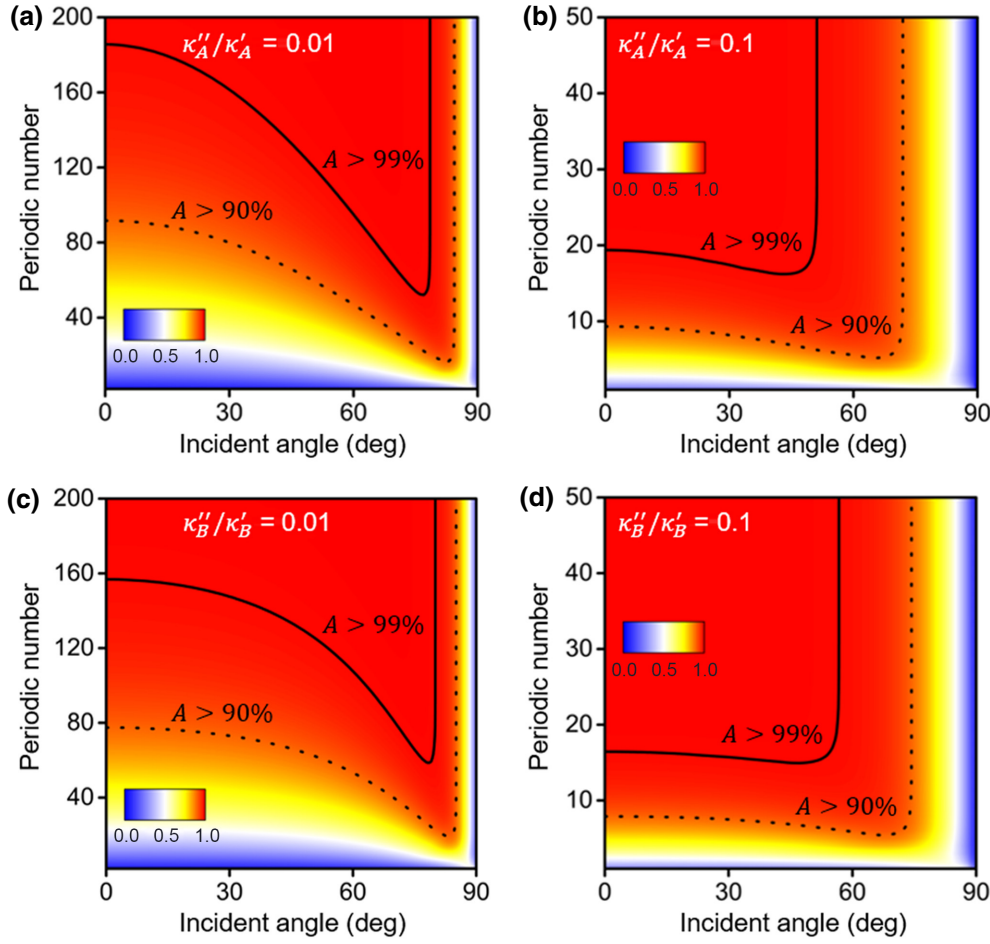


FIG. 3. 2D color maps for absorptance as a function of incident angles and multilayer periodic numbers with different material losses of (a) $\kappa''_A/\kappa'_A = 0.01$, (b) $\kappa''_A/\kappa'_A = 0.1$, (c) $\kappa''_B/\kappa'_B = 0.01$, and (d) $\kappa''_B/\kappa'_B = 0.1$. Region of absorptance above 99% (90%) is highlighted by the black solid (dotted) line. Working frequency is chosen as $fa/c_0 = 0.393$. Other parameters are $\rho_A = 1040 \text{ kg/m}^3$, $\kappa'_A = 1.2 \times 10^9 \text{ Pa}$, $\rho_B = 1039 \text{ kg/m}^3$, and $\kappa'_B = 2.8 \times 10^8 \text{ Pa}$. Bulk modulus, κ , is defined as $\kappa = \rho c^2$.

effective impedance of the composite is well matched with water over a large range of k_y at a single frequency (e.g., $fa/c_0 = 0.393$, olive dashed-dotted line), and the large k_y range suggests a large range of incident angles. The other result is that the region of matched impedance (blue color) is large enough that the property is broadband. The effective impedance of the composite can be obtained from $Z_{ABA} = \langle p \rangle / \langle v_x \rangle$, where p and v_x , respectively, are the eigenpressure and x -direction eigenvelocity. $\langle \dots \rangle$ represents the average eigenfield along the unit-cell boundary [45,46]. Thus, the broadband and wide-angle impedance matching is realized by the multilayer composite. In addition, such shifted spatial dispersions are accompanied by the spatially dispersive effective parameters shown in Fig. 2(c). These effective parameters can be retrieved from the eigenfields as $\rho_{\text{eff},x} = (k_x/\omega) \langle p \rangle / \langle v_x \rangle$, $\rho_{\text{eff},y} = (k_y/\omega) \langle p \rangle / \langle v_y \rangle$, and $1/\kappa_{\text{eff}} = (k_x/\omega) \langle v_x \rangle / \langle p \rangle + (k_y/\omega) \langle v_y \rangle / \langle p \rangle$, where $\langle v_y \rangle$ is the y -direction eigenvelocity [45,46].

To verify such a unique impedance-matching property, the transmittance spectra are recorded, as plotted in Figs. 2(d) and 2(e). Ten unit cells are considered in the simulations. It is seen that near-total (>99%) transmittance is achieved in an omnidirectional range of 0° – 86° at $fa/c_0 =$

0.393 in Fig. 2(d). In addition, high transmittance within a wide-incident-angle range is also realized at different frequencies of $fa/c_0 = 0.4$ and 0.41 . An example of acoustic pressure field distribution is plotted in the inset, demonstrating the effectiveness of impedance matching. Moreover, a 2D color map of transmittance as a function of the incident angles and frequencies is shown in Fig. 2(e), further demonstrating the broadband and wide-incident-angle impedance-matching property.

It should be pointed out that such a multilayer composite is optimized by an iterative algorithm, which is mainly focused on the optimization of the widest incident-angle range. Given the material parameters of A and B, we begin with a symmetric structure (ABA) and select the optimized solution with a maximum incident-angle range by adjusting the layer thickness of materials A and B at a particular frequency. In addition, one may obtain a broader bandwidth solution through an iterative algorithm focused on optimization of the bandwidth.

III. NEAR-TOTAL ABSORPTION

Based on the broadband and wide-incident-angle impedance-matching property discussed above, a loss factor is introduced to realize near-total absorption. First, we

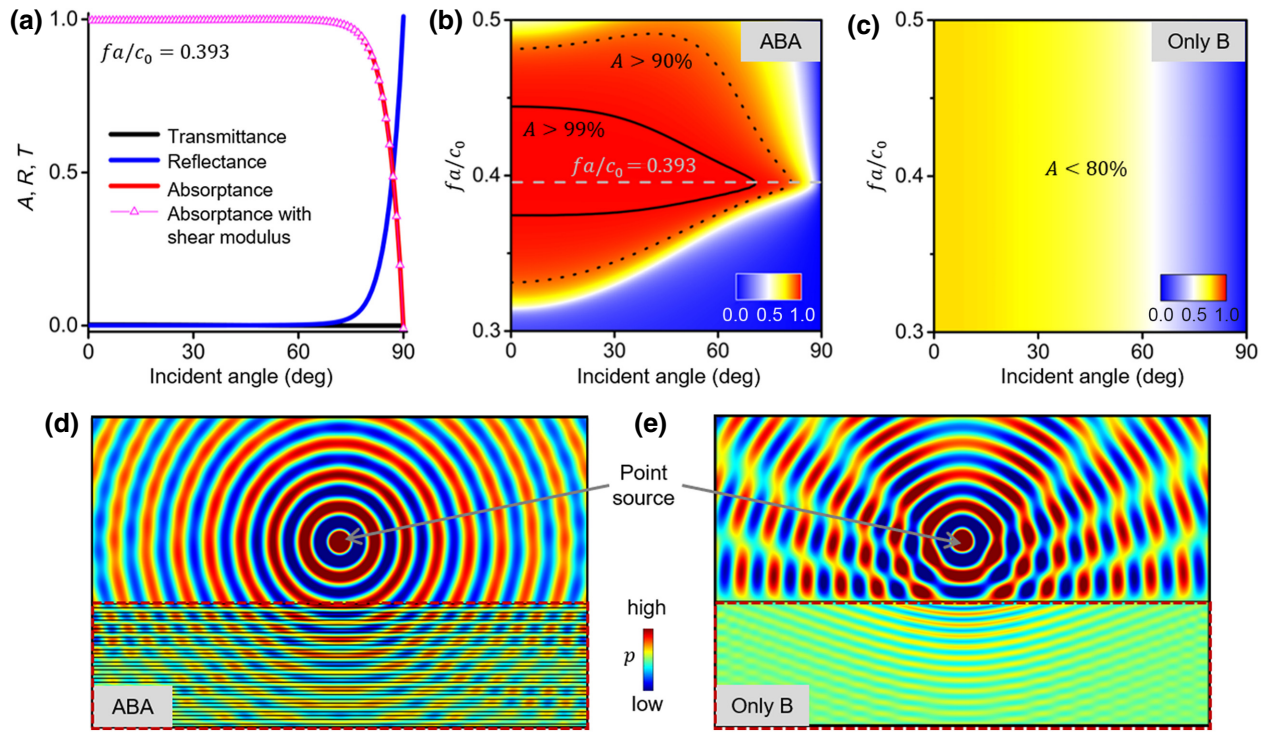


FIG. 4. Acoustic performances for an optimized absorber. Parameters are $\kappa''_A/\kappa'_A = 0.001$, $\kappa''_B/\kappa'_B = 0.038$, and $N = 50$ unit cells. (a) Absorptance, reflectance, and transmittance as a function of incident angles at $fa/c_0 = 0.393$. Absorptance calculated by an acoustic structure coupled model is also plotted as magenta symbols. Shear modulus of material A (B) is set as $G_A = 3 \times 10^5$ Pa ($G_B = 3 \times 10^5$ Pa) [50]. 2D color maps for absorptance as a function of incident angles and frequencies for (b) absorber and (c) comparison with only B materials. Pressure-field distributions under point-source radiation at $fa/c_0 = 0.393$ for (d) absorber and (e) comparison.

suppose only material A is absorptive. The bulk modulus of material A is rewritten as $\kappa_A = \kappa'_A - i\kappa''_A$, where κ'_A and κ''_A , respectively, represent the real and imaginary parts, and the imaginary part presents the loss. The 2D color maps of absorptance as a function of the incident angles and the multilayer periodic numbers with different amounts of loss are, respectively, plotted in Figs. 3(a) and 3(b). Obviously, as the periodic number increases, the absorptance rises accordingly. When the loss factor is small, $\kappa''_A/\kappa'_A = 0.01$, in Fig. 3(a), a large absorption of $A > 90\%$ with a near-omnidirectional incident-angle range of $0^\circ\text{--}84^\circ$ is obtained with a periodic number of 92, and a near-total absorption of $A > 99\%$ with a large angle range of $0^\circ\text{--}78^\circ$ is obtained with a periodic number of 186. When the loss factor increases to $\kappa''_A/\kappa'_A = 0.1$ in Fig. 3(b), the absorptance of $A > 90\%$ ($A > 99\%$) with an angle range of $0^\circ\text{--}71^\circ$ ($0^\circ\text{--}51^\circ$) and a periodic number of 10 (20) is obtained. Compared to the case of small loss ($\kappa''_A/\kappa'_A = 0.01$), the required periodic number for good absorption performance with a large loss factor ($\kappa''_A/\kappa'_A = 0.1$) obviously goes down, but this is accompanied by a trade-off that the incident-angle range narrows. In addition, there is a limit to the maximum incident angle for the large absorption when there is a sufficient periodic number.

Then, we suppose only material B is absorptive. Similarly, the bulk modulus of material B is rewritten as $\kappa_B = \kappa'_B - i\kappa''_B$. The corresponding results of absorptance spectra are plotted in Figs. 3(c) and 3(d). In the case of $\kappa''_B/\kappa'_B = 0.01$, $A > 90\%$ ($A > 99\%$) with $0^\circ\text{--}85^\circ$ ($0^\circ\text{--}80^\circ$) is achieved with a periodic number of 78 (157). In the case of $\kappa''_B/\kappa'_B = 0.1$, $A > 90\%$ ($A > 99\%$) with $0^\circ\text{--}74^\circ$ ($0^\circ\text{--}56^\circ$) is achieved with a periodic number of 8 (17). Similar conclusions can be obtained to those for the case of material A. A minor discrepancy between the two cases can be attributed to differences in the bulk modulus and layer thickness. Thus, a larger loss factor can make a thinner absorber but reduce the range of incident angles.

To obtain a balance between the maximum angle range and the multilayer composite thickness, an optimized absorber is exhibited based on the design in Fig. 2. The absorber is composed of absorptive material A with $\kappa''_B/\kappa'_B = 0.001$ and absorptive material B with $\kappa''_A/\kappa'_A = 0.038$. The multilayer periodic number, N , is chosen to be 50. Figure 4(a) shows the absorptance, reflectance, and transmittance as a function of the incident angles at $fa/c_0 = 0.393$ for the absorber. It is seen that near-total absorptance ($> 99\%$) is implemented within a large incident-angle range of $0^\circ\text{--}70^\circ$. When the incident angle

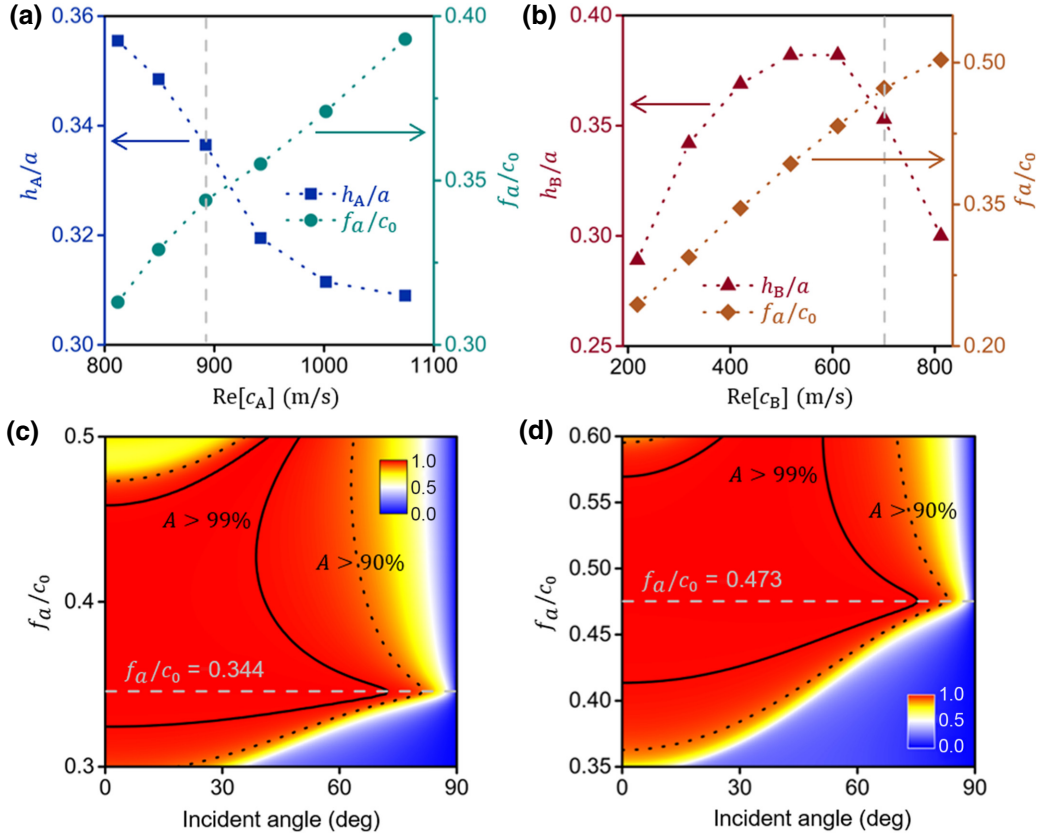


FIG. 5. Demonstration of the robustness of the absorber. (a) Alternative thickness of material A and working frequency for wide-incident-angle and high absorption with variation of the velocity of material A. (b) 2D color map for absorptance versus incident angles and frequencies for an example with $h_A/a = 0.3365$, $\rho_A = 1039.8 \text{ kg/m}^3$, $\text{Re}[c_A] = 892.1 \text{ m/s}$, $\kappa_A''/\kappa_A' = 0.001$, $h_B/a = 0.327$, $\rho_B = 1039 \text{ kg/m}^3$, $\text{Re}[c_B] = 518 \text{ m/s}$, $\kappa_B''/\kappa_B' = 0.069$, and $N = 50$. (c) Alternative thickness of material B and working frequency for wide-incident-angle and high absorption with variation of the velocity of material B. (d) 2D color map of absorptance versus incident angles and frequencies for an example with $h_B/a = 0.353$, $\rho_B = 1039.5 \text{ kg/m}^3$, $\text{Re}[c_B] = 700.7 \text{ m/s}$, $\kappa_B''/\kappa_B' = 0.067$, $h_A/a = 0.3235$, $\rho_A = 1040 \text{ kg/m}^3$, $\text{Re}[c_A] = 1074 \text{ m/s}$, $\kappa_A''/\kappa_A' = 0.001$, and $N = 50$.

increases over 70° , the reflectance gradually increases due to the result of impedance mismatching. At all incident angles, the transmittance remains zero. To clarify that the small shear modulus is negligible in our system, an acoustic structure coupled model is built. The results for absorptance are plotted as magenta symbols in Fig. 4(a); these results match well with those of the acoustic model, which are shown as the red solid line. From a 2D color map of the absorptance spectra plotted in Fig. 4(b), the unique property of wide-angle and large absorption is effective within a broad bandwidth from $f_a/c_0 = 0.33$ to 0.48 . For comparison in Fig. 4(c), the case of a slab made up of only material B with the same thickness can only realize a maximum absorptance below 80% under normal incidence. Moreover, the acoustic pressure fields under point-source radiation for the designed absorber and the comparison are, respectively, shown in Figs. 4(d) and 4(e), demonstrating the wide-angle characteristic of the near-perfect absorber. From Fig. 4(d), it is seen that the cylindrical waves impinge on the absorber and gradually vanish inside

the absorber. A near-perfect cylindrical wave field confirms the wide-angle impedance-matching property. For the comparison in Fig. 4(e), a chaotic field indicates a large reflection induced by impedance mismatching.

IV. ROBUSTNESS TO MATERIAL PARAMETERS

It should be noted that our method to implement the absorber based on broadband and wide-angle impedance matching is general and robust, and the selection of the material parameters discussed above is not a unique solution. To prove this, we redesign a variety of examples by choosing different material parameters. Figure 5(a) shows the parameter combination for the absorber with variation of material A with a fixed material B of $\rho_B = 1039 \text{ kg/m}^3$ and $\text{Re}[c_B] = 518 \text{ m/s}$. Obviously, as the real part of the velocity ($\text{Re}[c_A]$) changes, the thickness (h_A/a) and the working frequency (f_a/c_0) for the near-total absorption changes accordingly. Figure 5(b) shows the 2D map of absorptance as a function of the incident angles and the

frequencies for one example, as marked by the vertical dashed line in Fig. 5(a). A large incident-angle range of $0^\circ\text{--}72^\circ$ ($0^\circ\text{--}82^\circ$) for $A > 99\%$ ($A > 90\%$) is achieved at $fa/c_0 = 0.344$, and the wide-angle and high absorption is effective within a large bandwidth from $fa/c_0 = 0.32$ to -0.46 . Moreover, Figs. 5(c) and 5(d) show the results for the variation of material B with a fixed material A of $\rho_A = 1040 \text{ kg/m}^3$ and $\text{Re}[c_A] = 1074 \text{ m/s}$. From the example marked by the vertical dashed line in Fig. 5(c), a large incident-angle range of $0^\circ\text{--}75^\circ$ ($0^\circ\text{--}83^\circ$) for $A > 99\%$ ($A > 90\%$) at $fa/c_0 = 0.473$ and a large bandwidth of $fa/c_0 = 0.41 - 0.57$ for the wide-angle and high absorption is realized, as shown in Fig. 5(d). The flexibility of the composite material parameters guarantees that our method is general and robust.

V. CONCLUSION

We prove a general and robust method to design a kind of hydroacoustic absorber with high absorptance over a wide range of incident angles and a broad frequency spectrum. The proposed absorber, made up of flat multilayer composites with porous soft silicone rubber, possessing spatially dispersive effective parameters, is near-omnidirectional and perfectly impedance-matched with water. With a proper material loss, all the sound energy can be gradually dissipated inside the absorber. Good performances of absorption and flexibility in material parameters could promise useful underwater applications.

VI. METHODS

Numerical simulations are performed by using COMSOL Multiphysics, a finite-element analysis and solver software. Most simulations are performed in the pressure acoustic module, except for the magenta symbol line in Fig. 4(a), which is performed in the acoustic-solid interaction module. Periodic boundaries are set in Figs. 2, 3, 4(a)–4(c), and 5. Perfectly matched layers are set around the domain in Figs. 3(d) and 3(e). The parameters of the background medium, water, are set as $\rho_0 = 1000 \text{ kg/m}^3$ and $c_0 = 1483 \text{ m/s}$. The parameters of the porous silicone rubber are reported to be $\rho \approx (1 - \phi)\rho_0$, $c_L \approx c_L^0/\sqrt{1 + 3K_0\phi/4G_0}$, $c_T \approx c_T^0/\sqrt{1 + 2\phi/3}$, $c_L^0 \approx \sqrt{K_0/\rho_0}$, and $c_T^0 \approx \sqrt{G_0/\rho_0}$ in the literature [47–50], where $\rho_0 = 1040 \text{ kg/m}^3$, $K_0 = 1.2 \text{ GPa}$, and $G_0 = 0.3 \text{ MPa}$. The air-filling ratio, ϕ , for material A (B) is 0% (0.11%) in Figs. 2–4.

ACKNOWLEDGMENTS

This work is supported by the National Key R&D Program of China (Grant No. 2020YFA0211400) and the National Natural Science Foundation of China (Grants No. 11974176, No. 12174188, and No. 12174192).

- [1] H. Bai, Z. Zhan, J. Liu, and Z. Ren, From local structure to overall performance: An overview on the design of an acoustic coating, *Materials* **12**, 2509 (2019).
- [2] J. Dong and P. Tian, Review of underwater sound absorption materials, *IOP Conf. Ser. Earth Environ. Sci.* **508**, 012182 (2020).
- [3] Y. Wang, X. Miao, H. Jiang, M. Chen, Y. Liu, W. Xu, and D. Meng, Review on underwater sound absorption materials and mechanisms (in Chinese), *Adv. Mech.* **47**, 92 (2017).
- [4] Y. Zhang, K. Chen, X. Hao, and Y. Cheng, A review of underwater acoustic metamaterials (in Chinese), *Chin. Sci. Bull.* **65**, 1396 (2020).
- [5] Y. Fu, I. I. Kabir, G. H. Yeoh, and Z. Peng, A review on polymer-based materials for underwater sound absorption, *Polym. Test.* **96**, 107115 (2021).
- [6] L. H. Sperling, *Sound and Vibration Damping with Polymers: Basic Viscoelastic Definitions and Concepts* (ACS Publ., Washington, DC, 1990).
- [7] B. Li, H. Zhou, and G. Huang, A novel impedance matching material derived from polymer micro-particles, *J. Mater. Sci.* **42**, 199 (2007).
- [8] C. Guiping, H. Deping, and S. Guangji, Underwater sound absorption property of porous aluminum, *Colloids Surf., A* **179**, 191 (2001).
- [9] X. Wang, Porous metal absorbers for underwater sound, *J. Acoust. Soc. Am.* **122**, 2626 (2007).
- [10] H. Jiang and Y. Wang, Phononic glass: A robust acoustic-absorption material, *J. Acoust. Soc. Am.* **132**, 694 (2012).
- [11] W. Xu, C. Jiang, and J. Zhang, Underwater acoustic absorption of air-saturated open-celled silicon carbide foam, *Colloids Surf., A* **471**, 153 (2015).
- [12] M. Álvarez-Láinez, M. A. Rodríguez-Pérez, and J. A. De Saja, Acoustic absorption coefficient of open-cell polyolefin-based foams, *Mater. Lett.* **121**, 26 (2014).
- [13] R. X. Liu, D. L. Pei, and Y. R. Wang, Experimental research on sound absorption properties of impedance gradient composite with multiphase, *IOP Conf. Ser. Mater. Sci. Eng.* **733**, 012009 (2020).
- [14] X. Ren, J. Wang, G. Sun, S. Zhou, J. Liu, and S. Han, Effects of structural design including cellular structure precision controlling and sharp holes introducing on sound absorption behavior of polyimide foam, *Polym. Test.* **84**, 106393 (2020).
- [15] S. Ghaffari Mosanenzadeh, H. E. Naguib, C. B. Park, and N. Atalla, Design and development of novel bio-based functionally graded foams for enhanced acoustic capabilities, *J. Mater. Sci.* **50**, 1248 (2015).
- [16] G. Gaunaurd, One-dimensional model for acoustic absorption in a viscoelastic medium containing short cylindrical cavities, *J. Acoust. Soc. Am.* **62**, 298 (1977).
- [17] S. M. Ivansson, Sound absorption by viscoelastic coatings with periodically distributed cavities, *J. Acoust. Soc. Am.* **119**, 3558 (2006).
- [18] D. C. Calvo, A. L. Thangawng, C. N. Layman, R. Casalini, and S. F. Othman, Underwater sound transmission through arrays of disk cavities in a soft elastic medium, *J. Acoust. Soc. Am.* **138**, 2537 (2015).
- [19] V. Leroy, A. Strybulevych, M. Lanoy, F. Lemoult, A. Tourin, and J. H. Page, Superabsorption of acoustic waves with bubble metascreens, *Phys. Rev. B* **91**, 020301(R) (2015).

- [20] S. H. Sohrabi and M. J. Ketabdari, Numerical simulation of a viscoelastic sound absorbent coating with a doubly periodic array of cavities, *Cogent Eng.* **5**, 1529721 (2018).
- [21] G. S. Sharma, A. Skvortsov, I. MacGillivray, and N. Kessissoglou, Sound transmission through a periodically voided soft elastic medium submerged in water, *Wave Motion* **70**, 101 (2017).
- [22] M. Tao, H. Ye, and X. Zhao, Acoustic performance prediction of anechoic layer using identified viscoelastic parameters, *J. Vib. Control* **25**, 1164 (2019).
- [23] L. Huang, Y. Xiao, J. Wen, H. Zhang, and X. Wen, Optimization of decoupling performance of underwater acoustic coating with cavities via equivalent fluid model, *J. Sound Vib.* **426**, 244 (2018).
- [24] D. Zhao, H. Zhao, H. Yang, and J. Wen, Optimization and mechanism of acoustic absorption of Alberich coatings on a steel plate in water, *Appl. Acoust.* **140**, 183 (2018).
- [25] F. Zhou, J. Fan, B. Wang, and Z. Peng, Absorption performance of an anechoic layer with a steel plate backing at oblique incidence, *Acoust. Aust.* **46**, 317 (2018).
- [26] H. G. Zhao, Y. Z. Liu, J. H. Wen, D. L. Yu, and X. S. Wen, Tri-component phononic crystals for underwater anechoic coatings, *Phys. Lett. A: Gen. At. Solid State Phys.* **367**, 224 (2007).
- [27] P. Méresse, C. Audoly, C. Croënne, and A. C. Hladky-Hennion, Acoustic coatings for maritime systems applications using resonant phenomena, *C. R. Mec.* **343**, 645 (2015).
- [28] J. Wen, H. Zhao, L. Lv, B. Yuan, G. Wang, and X. Wen, Effects of locally resonant modes on underwater sound absorption in viscoelastic materials, *J. Acoust. Soc. Am.* **130**, 1201 (2011).
- [29] H. Jiang, Y. Wang, M. Zhang, Y. Hu, D. Lan, Y. Zhang, and B. Wei, Locally resonant phononic woodpile: A wide band anomalous underwater acoustic absorbing material, *Appl. Phys. Lett.* **95**, 104101 (2009).
- [30] J. Zhong, J. H. Wen, H. G. Zhao, J. F. Yin, and H. Bin Yang, Effects of core position of locally resonant scatterers on low-frequency acoustic absorption in viscoelastic panel, *Chin. Phys. B* **24**, 084301 (2015).
- [31] K. Shi, G. Jin, R. Liu, T. Ye, and Y. Xue, Underwater sound absorption performance of acoustic metamaterials with multilayered locally resonant scatterers, *Results Phys.* **12**, 132 (2019).
- [32] N. Gao and Y. Zhang, A low frequency underwater metastructure composed by helix metal and viscoelastic damping rubber, *J. Vib. Control* **25**, 538 (2019).
- [33] G. S. Sharma, A. Skvortsov, I. MacGillivray, and N. Kessissoglou, Sound absorption by rubber coatings with periodic voids and hard inclusions, *Appl. Acoust.* **143**, 200 (2019).
- [34] W. Wang and P. J. Thomas, Low-frequency active noise control of an underwater large-scale structure with distributed giant magnetostrictive actuators, *Sens. Actuators, A* **263**, 113 (2017).
- [35] Y. Sun, Z. Li, A. Huang, and Q. Li, Semi-active control of piezoelectric coating's underwater sound absorption by combining design of the shunt impedances, *J. Sound Vib.* **355**, 19 (2015).
- [36] Z. Zhang, Y. Huang, and Q. Huang, Low-frequency broadband absorption of underwater composite anechoic coating with periodic subwavelength arrays of shunted piezoelectric patches, *Compos. Struct.* **216**, 449 (2019).
- [37] M. A. Trindade and A. Benjeddou, Hybrid active-passive damping treatments using viscoelastic and piezoelectric materials: Review and assessment, *J. Vib. Control* **8**, 699 (2002).
- [38] Y. Duan, J. Luo, G. Wang, Z. H. Hang, B. Hou, J. Li, P. Sheng, and Y. Lai, Theoretical requirements for broadband perfect absorption of acoustic waves by ultra-thin elastic meta-films, *Sci. Rep.* **5**, 1038 (2015).
- [39] J. Mei, X. Zhang, and Y. Wu, Ultrathin metasurface with high absorptance for waterborne sound, *J. Appl. Phys.* **123**, 091710 (2018).
- [40] Y. Gu, H. Long, Y. Cheng, M. Deng, and X. Liu, Ultrathin Composite Metasurface for Absorbing Subkilohertz Low-Frequency Underwater Sound, *Phys. Rev. Appl.* **16**, 014021 (2021).
- [41] J. Luo, Y. Yang, Z. Yao, W. Lu, B. Hou, Z. H. Hang, C. T. Chan, and Y. Lai, Ultratransparent Media and Transformation Optics with Shifted Spatial Dispersions, *Phys. Rev. Lett.* **117**, 223901 (2016).
- [42] Z. Yao, J. Luo, and Y. Lai, Photonic crystals with broadband, wide-angle, and polarization-insensitive transparency, *Opt. Lett.* **41**, 5106 (2016).
- [43] Z. Yao, J. Luo, and Y. Lai, Illusion optics via one-dimensional ultratransparent photonic crystals with shifted spatial dispersions, *Opt. Express* **25**, 30931 (2017).
- [44] J. Luo and Y. Lai, Near-perfect absorption by photonic crystals with a broadband and omnidirectional impedance-matching property, *Opt. Express* **27**, 15800 (2019).
- [45] C. Liu, J. Luo, and Y. Lai, Acoustic metamaterials with broadband and wide-angle impedance matching, *Phys. Rev. Mater.* **2**, 045201 (2018).
- [46] C. Liu, C. Ma, X. Li, J. Luo, N. X. Fang, and Y. Lai, Wide-Angle Broadband Nonreflecting Acoustic Metamaterial Fence, *Phys. Rev. Appl.* **13**, 054012 (2020).
- [47] T. Brunet, J. Leng, and O. Mondain-Monval, Soft acoustic metamaterials, *Science* **342**, 323 (2013).
- [48] T. Brunet, A. Merlin, B. Mascaró, K. Zimny, J. Leng, O. Poncelet, C. Aristégui, and O. Mondain-Monval, Soft 3D acoustic metamaterial with negative index, *Nat. Mater.* **14**, 384 (2015).
- [49] C. Liu, P. Bai, and Y. Lai, Sound-impenetrable holes in water based on acoustic complementary medium, *EPL* **115**, 58002 (2016).
- [50] A. Ba, A. Kovalenko, C. Aristégui, O. Mondain-Monval, and T. Brunet, Soft porous silicone rubbers with ultra-low sound speeds in acoustic metamaterials, *Sci. Rep.* **7**, 40106 (2017).
- [51] J. Li and C. T. Chan, Double-negative acoustic metamaterial, *Phys. Rev. E* **70**, 055602 (2004).